Chemical Science

ROYAL SOCIETY OF CHEMISTRY

EDGE ARTICLE

View Article Online
View Journal | View Issue

Cite this: *Chem. Sci.*, 2025, **16**, 9679

All publication charges for this article have been paid for by the Royal Society of Chemistry

A universal strategy for bridging Prussian blue analogues and sodium layered oxide cathodes: direct fast conversion, dynamic structural evolution, and sodium storage mechanisms†

Hong-Wei Li,[abc] Jingqiang Wang,[*d] Jing Yu,[d] Jia-Yang Li,[ab] Yan-Fang Zhu,[*abf] Huanhuan Dong,[ab] Zhijia Zhang,[*c] Yong Jiang,[c] Shi-Xue Dou[e] and Yao Xiao[*abf]

Prussian blue analogues (PBAs) are widely recognized as one of the most promising cathode materials for sodium-ion batteries (SIBs). However, many unqualified PBAs with unsatisfactory electrochemical performance are difficult to dispose of and pose a risk of environmental contamination. Additionally, the production process of layered oxides, another popular cathode material for SIBs, requires prolonged high-temperature sintering, resulting in significant energy consumption. To address the aforementioned issues, a "two birds with one stone" strategy is proposed. This approach not only demonstrates the feasibility of directly preparing layered oxides with PBAs as precursors through a fast sintering process but also simultaneously addresses the challenge of treating unqualified PBAs while minimizing excessive energy consumption during the preparation of layered oxides. Furthermore, a series of binary, ternary, and quaternary layered oxides were synthesized directly by utilizing PBAs with varying compositions, showcasing the universality of this strategy. This innovative approach breaks the boundaries between different types of sodium cathode materials and builds a distinctive bridge for the direct conversion of PBAs into layered oxides, thereby widening the feasibility of the cathode for SIBs.

Received 26th February 2025
Accepted 4th April 2025

DOI: 10.1039/d5sc01550b

rsc.li/chemical-science

Introduction

Environmental pollution and climate change increasingly necessitate the substitution of traditional fossil fuels with sustainable and clean energy sources.[1,2] Recently, the worldwide utilization of solar and wind energy has surged dramatically; however integrating the power generated by these intermittent renewable sources into large-scale grids presents significant challenges. Consequently, the development of energy storage technologies has become urgently necessary.[3,4] Compared to mechanical, thermal, and hydrogen energy storage systems, secondary battery energy storage systems are prioritized in new energy storage applications due to their lack of geographical constraints, lower costs, and higher efficiency.[5–12] Among them, lithium-ion batteries (LIBs) are struggling to meet the growing demand for energy storage due to limited lithium resources. In contrast, sodium-ion batteries (SIBs), which utilize abundant sodium resources, present a viable alternative to new energy storage systems.[13–16] SIBs that employ Prussian blue analogues (PBAs) and transition metal layered oxides as cathodes are widely adopted because of their high theoretical specific capacity, low cost, and simple preparation method.[17–20]

PBAs cathode systems have been extensively studied by many world-renowned SIB companies such as Natron Energy (US), Altris (SE), HiNa, CATL (CN), *etc.* Logically, a significant yield of unqualified PBAs arises during the optimization process of material preparation as it transitions from the laboratory scale to commercial production scale.[21] Owing to the intrinsic structural characteristics of –CN present in PBAs, the potential toxicity undoubtedly poses a considerable threat to the environment and human beings. Consequently, the disposal of these unqualified PBAs is a significant challenge.[22,23] Separately, since the early exploration of the Na^+ de-/intercalation behavior in $NaCoO_2$ during the 1980s, transition metal layered oxides have been extensively studied as prominent cathode materials for SIBs due to their high specific capacity and facile synthesis methods.[24–27] Typically, layered oxide cathodes are produced

[a]College of Chemistry and Materials Engineering, Wenzhou University, Wenzhou, 325035, China. E-mail: yanfangzhu@wzu.edu.cn; xiaoyao@wzu.edu.cn
[b]Wenzhou Key Laboratory of Sodium-Ion Batteries, Wenzhou University Technology Innovation Institute for Carbon Neutralization, Wenzhou 325035, China
[c]School of Materials Science and Engineering, Tiangong University, Tianjin 300387, China. E-mail: zhangzhijia@tiangong.edu.cn
[d]College of Chemistry and Chemical Engineering, Inner Mongolia University, Hohhot, Inner Mongolia 010021, China. E-mail: jqwangchi@hotmail.com
[e]Institute of Energy Materials Science (IEMS), University of Shanghai for Science and Technology, Shanghai 200093, China
[f]Key Laboratory of Advanced Energy Materials Chemistry (Ministry of Education), Nankai, Tianjin 300071, China

† Electronic supplementary information (ESI) available. See DOI: https://doi.org/10.1039/d5sc01550b

through high-temperature solid-state sintering of various reagents in stoichiometric ratios that correspond to the desired composition of the target product.[28–30] This process often results in significant energy consumption, requiring holding times of over ten hours. Therefore, it is important to explore a fast sintering strategy to reduce the energy consumption in the production of layered oxide cathodes for SIBs.[31] It would be very interesting and prospective if layered oxide cathodes could be synthesized through fast sintering of PBAs precursors, with transition metals and sodium ions uniformly distributed in the open skeletal structure of PBAs. This "two birds with one stone" strategy not only conserves substantial energy during the layered oxide production process but also addresses the issue of dealing with unqualified PBAs, thereby achieving both economic and environmental benefits.

Based on the discussion above, a straightforward strategy has been adopted to prepare layered oxide cathodes for SIBs using PBAs as precursors, and the applicability of the fast sintering strategy has been verified. Compared to the traditional solid-state method, the fast sintering strategy eliminates the need for precursor hybridization and reduces the high-temperature holding time from over 10 hours to just 10 minutes. All binary, ternary, and quaternary layered oxides produced from PBAs with different components, whether by the long period sintering or fast sintering method, exhibit favorable crystalline properties and excellent sodium storage performance. Furthermore, this innovative strategy allows for the disposal of unqualified PBAs, achieving waste reutilization while balancing economic and environmental benefits.[32–34] Additionally, the fast sintering technology significantly enhances production efficiency and reduces energy consumption. This process also mitigates potential pollution by converting waste materials into valuable products, thereby significantly lowering treatment costs and generating added economic value, making it highly attractive for industrial-scale applications. Take the quaternary Fe/Mn-based layered oxides produced through this fast sintering method for example. These oxides demonstrate a high specific capacity of 124.3 mAh g^{-1} at 0.1 C and exhibit excellent rate performance, achieving a capacity of 88.5 mAh g^{-1} at 2 C, as well as maintaining a capacity retention of 76.1% after 250 cycles at 1 C. The structural evolution from the PBAs to layered oxides was elucidated using *in situ* high-temperature X-ray diffraction (HTXRD). The remarkable reversibility of the layered oxide cathodes, prepared by the fast sintering of PBAs precursors, during sodium ion insertion and extraction was confirmed through *in situ* XRD. Collectively, these results validate the practicality and scalability of the method for directly fast sintering PBAs into layered oxides.

Results and discussion

As schematically illustrated in Fig. 1a, layered oxides with various phases can be tailored by modulating the composition

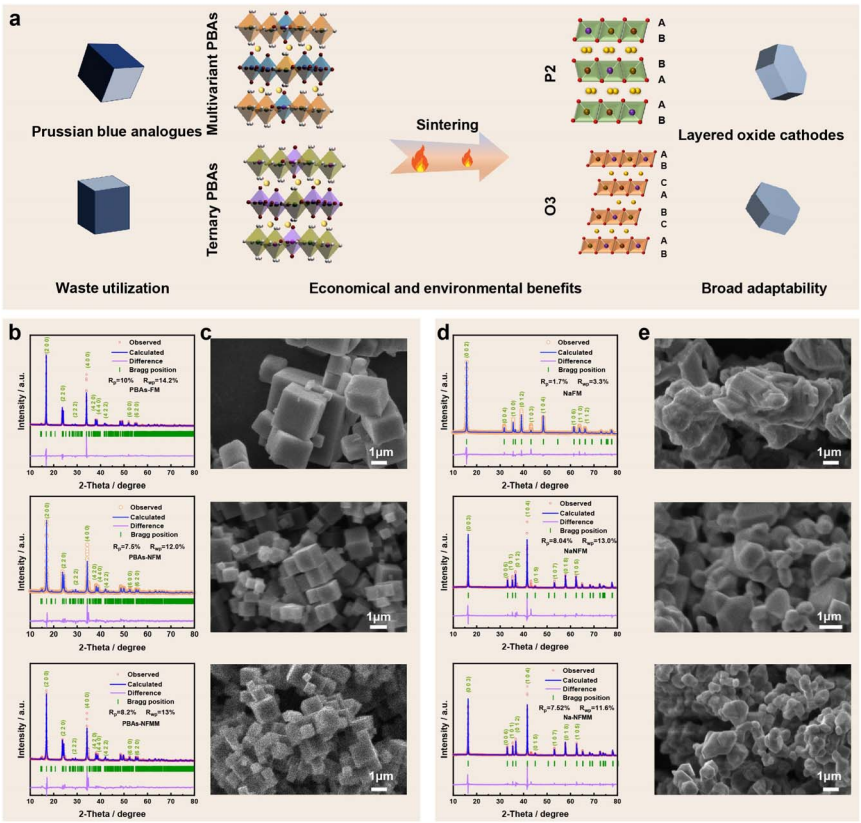

Fig. 1 (a) Schematic diagram of PBAs sintering conversion into layered oxides. (b) Rietveld refinement of the XRD results and (c) SEM images of PBAs-FM, PBAs-NFM, and PBAs-NFMM. (d) Rietveld refinement of the XRD results and (e) SEM images of NaFM, NaNFM, and NaNFMM.

of the PBAs precursors and controlling the sintering process. Herein, three distinct types of PBAs were designed and synthesized as the prototypes for the development of layered oxide cathodes for SIBs using the long period sintering method. Based on their composition, the binary (Fe/Mn-containing), ternary (Ni/Fe/Mn-containing), and quaternary (Ni/Fe/Mg/Mn-containing) PBAs are designated as PBAs-FM, PBAs-NFM, and PBAs-NFMM, respectively. The X-ray diffraction (XRD) patterns and Rietveld refinement results (Fig. S1a–c† and 1b) indicate that the binary, ternary, and quaternary PBAs exhibit favorable crystallinity, consistent with the standard peaks of the Prussian blue analogue (JCPDS card no. 82-1111),[35] and their cell parameters are summarized in Table S1.† The SEM images in Fig. 1c reveal that all the PBAs possess a uniform cubic morphology; however, the particle size decreases as the number of element types in the composition increases. Utilizing these three types of PBAs as precursors, layered oxides with P2 and O3 phases respectively can be obtained through the long period sintering method. According to the XRD pattern shown in Fig. S2a,† the characteristic peaks of $Na_{0.5}Fe_{0.5}Mn_{0.5}O_2$ (NaFM) derived from the binary PBAs-FM correspond to those of the P2-type layered oxide in the $P6_3/mmc$ space group (JCPDS card no. 27-0752).[36] However, when employing the same sintering procedure, the layered oxides of $Na_{0.8}Ni_{0.2}Fe_{0.5}Mn_{0.3}O_2$ (NaNFM) and $Na_{0.8}Ni_{0.15}Fe_{0.5}Mg_{0.05}Mn_{0.3}O_2$ (NaNFMM) obtained from the ternary PBAs-NFM and quaternary PBAs-NFMM precursors, respectively, exhibit the O3 phase within the $R\bar{3}m$ space group (JCPDS card no. 54-0887) (Fig. S2b and c†).[37] The prepared layered oxides with different phases are further validated by the Rietveld refinement of the XRD results (Fig. 1d), from which the specific cell parameters of NaFM, NaNFM, and NaNFMM can be derived, as shown in Table S2.† The SEM images in Fig. 1e illustrate that the morphology of NaFM, NaNFM, and NaNFMM all exhibit a hexagonal plate shape characteristic of layered oxides, with sizes comparable to their corresponding PBAs precursors. This similarity may be attributed to the confinement of atomic rearrangement and crystal growth within the distinct structure of PBAs during the long period sintering process.[38] Energy dispersive spectroscopy (EDS) elemental mapping of NaNFM and NaNFMM, presented in Fig. S3 and S4,† demonstrates a homogeneous distribution of elements without any segregation.

NaNFM was characterized in detail to verify the feasibility and beneficial effects of the strategy for directly converting PBAs into layered oxides using the long period sintering method. The crystalline structure of NaNFM was further investigated by employing high-resolution transmission electron microscopy (HRTEM). The TEM image in Fig. S5a† further confirms the hexagonal, plate-like layered structure of NaNFM, while the HRTEM images in Fig. S5b and c† reveal a lattice fringe spacing of 0.252 nm, which corresponds to the (101) facet of the O3 phase structure, as calculated using the Bragg equation ($2d \sin\theta = n\lambda$).[39] In addition, the chemical valence states of the transition metals in NaNFM were further investigated using X-ray photoelectron spectroscopy (XPS). As illustrated in Fig. S6,† the high-resolution Ni 2p spectra of the NaNFM can be deconvoluted into two peaks at 854.9 eV and 872.5 eV, which correspond to Ni^{2+}, along with two associated satellite peaks.[40] The high-resolution Fe 2p spectra reveal two pairs of peaks with binding energies of 709.9 eV and 723.1 eV, as well as 713.2 eV and 726.3 eV, corresponding to Fe^{2+} and Fe^{3+}, respectively, along with two satellite peaks.[41] Similarly, the binding energies of 641.1 eV and 652.3 eV corresponding to Mn^{4+}, are also observed in the high-resolution Mn 2p spectrum.[42,43] The presence of various valence states among these transition metal cations indicates their electrochemical activity, which ensures the capability to deliver high specific capacities in NaNFM derived from the PBAs-NFM precursor. Furthermore, in addition to the lattice oxygen peak with a binding energy of 529.3 eV in the high-resolution O 1s, there is a peak representing OH^-, which may result from unavoidable exposure to air during the XPS testing.[44,45] Likewise, as demonstrated by the XPS spectra in Fig. S7,† the chemical environment of the transition metals in NaNFMM is consistent with that of NaNFM.

To gain insight into the mechanisms underlying the transition from PBAs-NFM to NaNFM, an *in situ* high-temperature X-ray diffraction (HTXRD) test was conducted to monitor the dynamic sintering process of PBAs-NFM in an air atmosphere, ranging from 25 to 950 °C. As shown in Fig. 2a, the PBAs-NFM retain their original hexagonal structure from room temperature up to 200 °C (Fig. S8a†). And the gradually diminishing peaks at around 15° can be attributed to the removal of crystallization water from the PBAs-NFM as the temperature increases.[46] When the temperature reaches 300 °C, the well-defined crystalline structure of PBAs-NFM is destroyed, causing the atoms to escape the constraints of the lattice and become randomly arranged; additionally, the escape velocity of the lighter oxygen and sodium atoms exceeds that of the heavier transition metal atoms, resulting in an amorphous structure (Fig. S8b†). This amorphous state persists until the temperature increases to 480 °C, at which point the P2 phase begins to emerge. The crystal structure of the P2 phase progressively improves with increasing temperature, as evidenced by the enhanced intensity of the (002), (004), and (100) peaks at 15.4, 31.5, and 35.8°, respectively (Fig. S8c†). Notably, as the temperature continues to increase, the characteristic peaks at 16.0, 32.4, 34.8, and 40.9° corresponding to (003), (006), (101), and (104) crystal planes, respectively, of the O3 phase, gradually increase in intensity within the temperature range of 620–700 °C. This observation signifies the transition from the P2 phase to the O3 phase (Fig. S8d†). In the final stage of sintering, the characteristic peaks of the O3 phase in the temperature range of 760–950 °C become progressively sharper and more intense, indicating an improvement in the crystallinity of the O3 phase structure with increasing temperature (Fig. S8e†).[47] Ultimately, a well-crystallized O3 phase structure can be achieved after the temperature reaches 950 °C or upon cooling to 25 °C (Fig. S8f†). Furthermore, Fig. S9† and 2b present the *in situ* HTXRD patterns corresponding to the main characteristic diffraction peak intensity contour maps (bird's eye view), which further illustrate the phase transition from PBAs to layered oxides during the sintering process. Overall, as schematically depicted in Fig. 2c, the transformation of PBAs-NFM to NaNFM involves a structural evolution from PBAs to an amorphous state, and

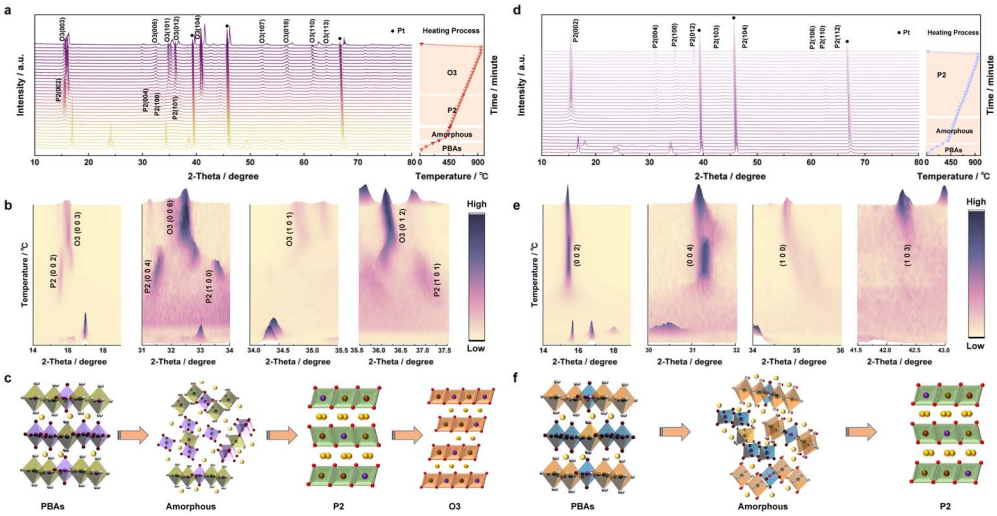

Fig. 2 *In situ* HTXRD patterns of the process (a) from PBAs-NFM to NaNFM and (d) from PBAs-FM to NaFM. The corresponding main characteristic diffraction peak intensity contour maps (bird's eye view) of the process (b) from PBAs-NFM to NaNFM and (e) from PBAs-FM to NaFM. Schematic diagram of the transformation process (c) from PBAs-NFM to NaNFM and (f) from PBAs-FM to NaFM.

subsequently, driven by thermodynamic factors, to the P2 phase and ultimately to the O3 structure. The structural transformation process of PBAs-NFMM precursors is similar to that of PBAs-NFM, maintaining the original structure except for the loss of crystallization water below 200 °C, then becoming amorphous between 300 and 460 °C, subsequently forming a P2-type layered oxide structure, with the characteristic peaks gradually intensifying within the temperature range of 480–560 °C. As the temperature continues to increase, the O3 phase gradually becomes the dominant phase, and the P2 phase completely disappears at 740 °C. Ultimately, the material transformed into a fully O3 phase after being sintered at 950 °C or cooled to 25 °C. The conversion process of PBAs-NFMM into the O3 phase layered oxide throughout the entire sintering process is illustrated in Fig. S10 and S11.† The HTXRD test was employed to investigate the formation process of the NaFM from the PBAs-FM precursor in an air atmosphere, with temperatures ranging from 25 to 950 °C (Fig. 2d). Similar to PBAs-NFM, the PBAs-FM can also retain the integrity of their crystal structure below 200 °C (Fig. S12a†). In the temperature range of 300 to 460 °C, organic structure decomposition occurs, resulting in a disordered atomic arrangement that exhibits an amorphous structure (Fig. S12b†). As the temperature increases to 480 °C, thermodynamic forces drive these disordered atoms into an entropy-stable ordered arrangement,[48] triggering a transition from the amorphous phase to the P2 phase. The P2 phase becomes progressively more refined as the temperature continues to increase (Fig. S12c and d†). Furthermore, the *in situ* HTXRD patterns, which correspond to the intensity contour maps of the main characteristic diffraction peaks shown in Fig. S13† and 2e, along with the schematic diagram of structural transformation in Fig. 2f, clearly illustrate this transformation process. These experimental results indicate that PBAs can be directly converted into layered oxide materials after undergoing a series of structural transformations.

To evaluate the practical feasibility of the strategy of sintering PBAs as precursors for the preparation of layered oxide cathodes for SIBs, electrochemical behavior tests were conducted in a half-cell with a potential window of 2–4 V. As illustrated in Fig. 3a and S14a,† the galvanostatic charge/discharge (GCD) profiles of NaNFM demonstrate a discharge capacity of 112.1 mAh g^{-1} and an energy density of 356.6 Wh kg^{-1} at 0.1 C, significantly surpassing those of the PBAs-NFM precursor, which exhibited a discharge capacity of 101.1 mAh g^{-1} and an energy density of 337.1 Wh kg^{-1}. The rate performance of NaNFM and PBAs-NFM precursors was evaluated over a current density range from 0.1 C to 2 C. Fig. 3b, c and S14b† demonstrate that NaNFM maintains a reversible specific capacity of 82.9 mAh g^{-1} at 2 C, which is 19.3 mAh g^{-1} higher than that of PBAs-NFM. Furthermore, the capacity retention of NaNFM at 2 C is 73.9%, surpassing that of PBAs-NFM. The cycling performance of both NaNFM and PBAs-NFM is depicted in Fig. 3d, S15a and b.† NaNFM exhibits a superior capacity retention of 89.5% after 100 cycles at 1 C with a coulombic efficiency of approximately 100% (compared to 82.9% for PBAs-NFM after 100 cycles). The electrochemical performance of NaNFMM, prepared through long period sintering of the PBAs-NFMM precursor, was also investigated. This material demonstrates a specific capacity of 125.6 mAh g^{-1} and an energy density of 397.1 Wh kg^{-1} at 0.1 C within the voltage window of 2–4 V (Fig. 3e and S16a†), which is roughly 24.1 mAh g^{-1} and 59.7 Wh kg^{-1} higher than those of the corresponding PBAs-NFMM precursors. As shown in Fig. 3f, g and S16b,† NaNFMM also exhibits an excellent rate performance, achieving a capacity retention of 71.5% and a specific capacity of 89.7 mAh g^{-1} at 2 C, higher than that of the PBAs-NFMM precursor. Furthermore, NaNFMM demonstrates both good capacity retention and a higher specific capacity than the PBAs-NFMM precursor over 100 cycles at 1 C (Fig. 3h, S17a and b†). Additionally, as shown in Fig. S18,† NaFM also exhibits superior

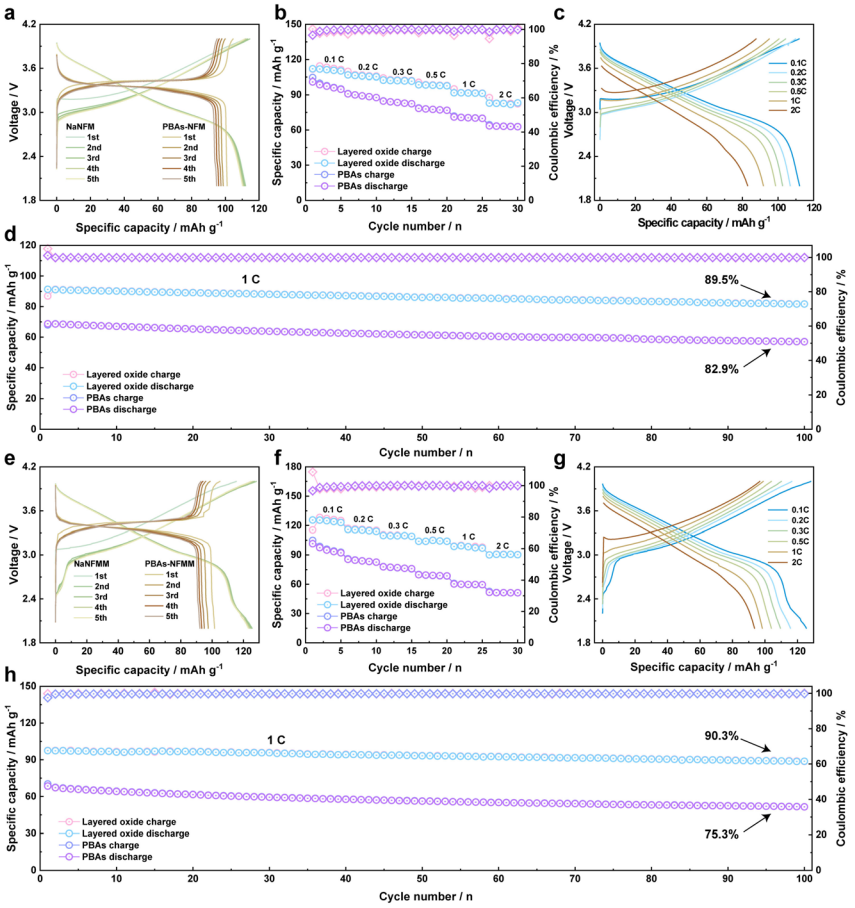

Fig. 3 Electrochemical performance within the potential window of 2–4 V: GCD curves at 0.1 C for (a) NaNFM and PBAs-NFM and (e) NaNFMM and PBAs-NFMM. Rate performance comparison of (b) NaNFM and PBAs-NFM and (f) NaNFMM and PBAs-NFMM. GCD curves at different rates of (c) NaNFM and (g) NaNFMM. Cycling performance comparison for (d) NaNFM and PBAs-NFM and (h) NaNFMM and PBAs-NFMM.

electrochemical performance compared to its PBAs-FM precursor. All of the above results suggest that utilizing PBAs as precursors for the preparation of layered oxide *via* the long period sintering method can achieve the purpose of improving electrochemical properties.

Compared to the direct physical mixing of various metal salts used as the raw materials in conventional solid-state sintering methods, precursor-based approaches have achieved an ordered arrangement of sodium and transition metal elements at the atomic level. This advancement allows for a significantly lower energy requirement to facilitate the formation of layered oxide crystals during high-temperature sintering.[49–51] Consequently, the strategy of fast sintering, which reduces the holding time at high temperatures, is feasible for the production of layered oxides utilizing PBAs as precursors (Fig. 4a). Unlike the conventional solid-state method, which necessitates maintaining the high-temperature for over 10 hours, the fast sintering strategy can reduce the holding time to just 10 minutes.[52,53] Motivated by this hypothesis, the fast sintering strategy was employed to produce layered oxides using PBAs-FM, PBAs-NFM, and PBAs-NFMM as precursors, respectively.

The layered oxide with the chemical formula of $Na_{0.55}Fe_{0.5}Mn_{0.5}O_2$ (NaFM-F) was synthesized using a fast sintering strategy with PBAs-FM as the precursor. The XRD pattern shown in Fig. S19a† indicates the P2-type phase of NaFM-F, and the crystal parameters derived from the Rietveld refinement results (Fig. S20a†) are presented in Table S3.† The SEM and TEM images in Fig. S20b and c† reveal that NaFM-F has a similar morphology but a smaller particle size compared to NaFM prepared *via* the long period sintering method. The clear lattice fringes in the HRTEM image (Fig. S20d and S21†) demonstrate that the lattice spacing of NaFM-F is 0.229 nm, corresponding to the (012) facet of the P2 structure. EDS mapping in Fig. S22† confirms the uniform distribution of Fe and Mn within the sample. The HRXPS spectra of Fe 2p, Mn 2p, and O 1s in Fig. S23a–c† indicate that NaFM-F possesses the same chemical valence as the NaFM, with Fe in the +2/+3 valence states, Mn in the +4 valences states and O existing as lattice-O and adsorbed OH^-. Similarly, the ternary compound $Na_{0.85}Ni_{0.2}Fe_{0.5}Mn_{0.3}O_2$ (NaNFM-F) was synthesized using ternary PBAs-NFM as the precursor through the fast sintering strategy. The XRD pattern (Fig. S19b†) and its Rietveld refinement results (Fig. 4b) indicate that the phase structure of NaNFM-F is the O3 type structure with crystal parameters $a = b = 2.98$ Å and $c = 16.16$ Å (Table S3†). NaNFM-F exhibits a smaller particle size compared to NaNFM, as shown in the SEM and TEM images (Fig. 4c and d).

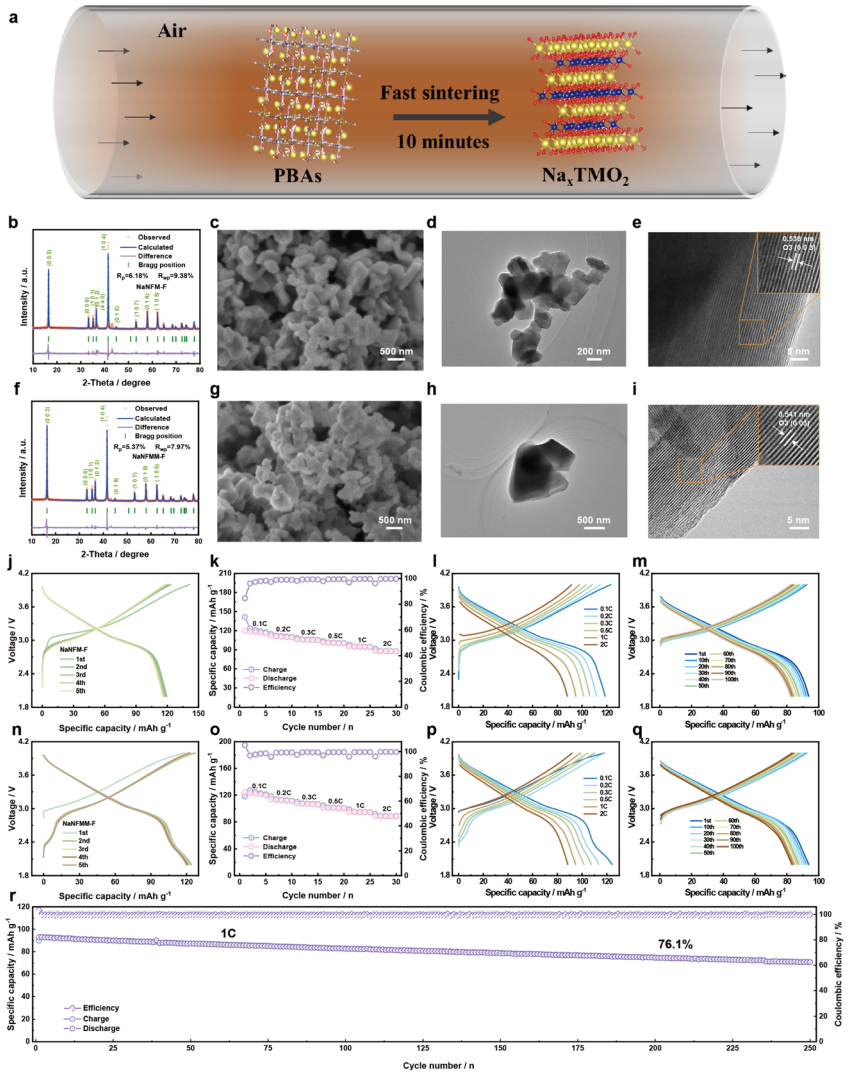

Fig. 4 (a) Schematic diagram of the transformation process from PBAs to layered oxides. (b) Powder XRD result with Rietveld refinement of NaNFM-F. (c) SEM, (d) TEM, and (e) HRTEM images of NaNFM-F. (f) Powder XRD result with Rietveld refinement of NaNFMM-F. (g) SEM image of NaNFMM-F. (h) TEM and (i) HRTEM images of NaNFMM-F. Electrochemical performance of the electrode within the potential window of 2–4 V: GCD curves at 0.1 C for (j) NaNFM-F and (n) NaNFMM-F. Rate performance of (k) NaNFM-F and (o) NaNFMM-F. GCD curves at different rates of (l) NaNFM-F and (p) NaNFMM-F. GCD curves at different cycles of (m) NaNFM-F and (q) NaNFMM-F. (r) Cycling performance of NaNFMM-F.

TEM-EDS mapping in Fig. S24† reveals a well-dispersed distribution of Ni, Fe, and Mn elements in NaNFM-F. The HRTEM images of NaNFM-F in Fig. 4e show a lattice fringe distance of 0.536 nm corresponds to the (003) crystal plane of the O3 phase. HRXPS spectra in Fig. S25a–d† suggest that the Ni, Fe, and Mn in NaNFM-F exist in the oxidation states of +2, +2/+3, and +4 respectively. The novel fast sintering strategy was also applied to quaternary PBAs-NFMM precursors to demonstrate its broad applicability. The resulting layered oxide, with the chemical formula $Na_{0.85}Ni_{0.15}Fe_{0.5}Mg_{0.05}Mn_{0.3}O_2$ (NaNFMM-F), exhibits the O3 phase structure within the $R\bar{3}m$ space group, with cell parameters $a = b = 2.97$ Å and $c = 16.21$ Å, as determined from the XRD pattern and Rietveld refinement results (Fig. 4f, S19c and Table S3†). Notably, similar to the binary NaFM-F and ternary NaNFM-F, the quaternary NaNFMM-F prepared using the fast sintering method has a smaller particle size compared to its counterparts obtained through the long period sintering method (Fig. 4g and h). This universal phenomenon can be attributed to the reduced high temperature holding time, which minimizes agglomeration during crystal growth. The EDS mapping in Fig. S26† demonstrates a uniform distribution of Na, Ni, Fe, Mg, Mn, and O in NaNFMM-F. The crystal structure of NaNFMM-F was further studied using the HRTEM images in Fig. 4i, where the lattice spacing of 0.541 nm corresponds to the (003) facets of the O3 structure. Consistent with these findings, the HRXPS spectra in Fig. S25e–g† indicate that Ni, Fe, and Mn in NaNFMM-F exist in the valence states of +2, +2/+3, and +4. Additionally, the HRXPS of O 1s in Fig. S25h† reveals a further reduction in the intensity of the adsorbed $(OH)^-$ compared to NaNFM-F, suggesting enhanced air stability of NaNFMM-F due to the substitution of Mg.

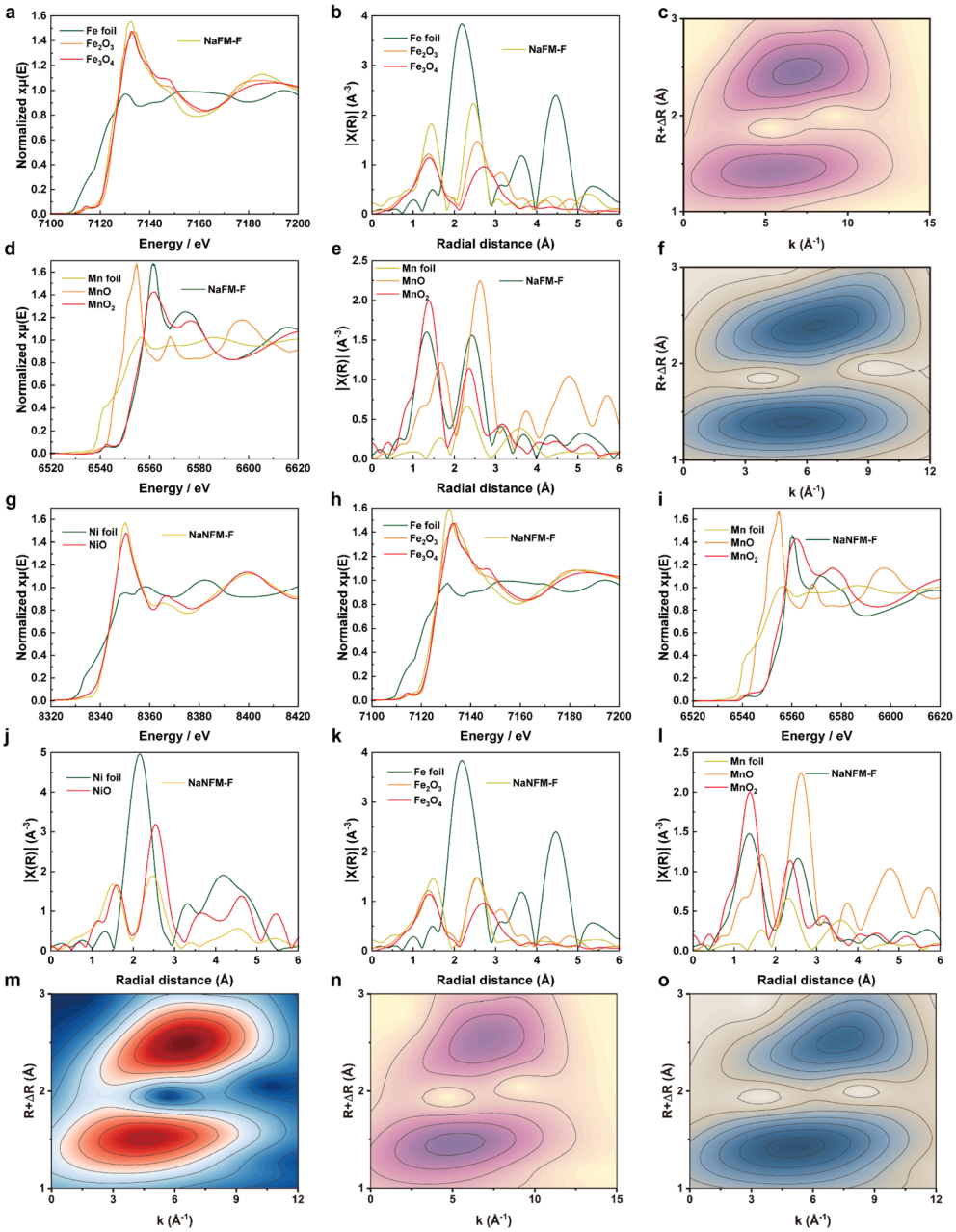

Fig. 5 XAS spectra of NaFM-F. (a and d) XANES spectra of Fe and Mn K-edge. (b and e) EXAFS spectra of Fe and Mn K-edge plotted in R space. (c and f) WT-EXAFS spectra of Fe and Mn K-edge. XAS spectra of NaNFM-F. (g–i) XANES spectra of Ni, Fe and Mn K-edge. (j–l) EXAFS spectra of Ni, Fe and Mn K-edge plotted in R space. (m–o) WT-EXAFS spectra of Ni, Fe and Mn K-edge.

For the practical application of the fast sintering strategy, investigations into the electrochemical properties are also necessary. The specific capacity of NaNFM-F is 119.6 mAh g^{-1} at 0.1 C (Fig. 4j), which is higher than that of NaNFM. This improvement is likely due to the increased number of active reaction sites resulting from the smaller particle size of the material, which increases the contact area with the electrolyte. Fig. 4k and l demonstrate that the specific capacity of NaNFM-F can reach up to 88.1 mAh g^{-1} even at 2 C, indicating a good rate performance. Interestingly, as shown in Fig. 4n, the quaternary NaNFMM-F exhibits a capacity of 124.3 mAh g^{-1}, slightly higher than that of NaNFM-F. This enhancement can be observed in the GCD profile of NaNFMM-F at approximately 2.1–2.4 V.[54] The satisfactory rate performance of NaNFMM-F, with a capacity of 88.5 mAh g^{-1} at 2 C, is illustrated in Fig. 4o and p. Similarly, Fig. S27† indicates that the binary NaFM-F also demonstrates good electrochemical properties comparable to those of NaFM obtained through the long period sintering method. Furthermore, benefiting from the "pillar effect" of a small amount of Mg substitution in the layered oxide occupying the Na site,[55] NaNFMM-F exhibits a capacity retention of 76.1% over 250 cycles at 1 C, which is superior to the 69.1% of Mg-free NaNFM-F (Fig. 4m, q, r, and S28†).

To investigate the charge compensation mechanism of the layered oxides synthesized through the fast sintering method, X-ray absorption fine structure (XAS) measurements were carried out to survey the chemical states and local atomic coordination environments of the elements in NaFM-F and NaNFM-F. The X-ray absorption near-edge structure (XANES) spectra at the Fe K-edges of NaFM-F and reference iron oxides are presented in Fig. 5a. Compared to Fe foil, the spectrum at the Fe K-edge of NaFM-F shifts to a higher energy, falling between the reference spectra of Fe_2O_3 and Fe_3O_4, and is closer to that of Fe_3O_4, manifesting that the valence state of Fe in NaFM-F is between +2 and +3.[56] The Fourier-transformed (FT) k^3-weighted extended X-ray absorption fine structure (EXAFS) spectra of the Fe atoms in NaFM-F are shown in Fig. 5b. There are two prominent peaks at approximately 1.42 and 2.48 Å, which can be attributed to Fe–O and Fe–TM bonds, respectively.[57] These results are consistent with the analyses of the corresponding Wavelet Transform (WT)-EXAFS spectra. In contrast to the single intensity maximum assigned to the Fe–Fe bonds in the WT-EXAFS spectra of Fe foil (Fig. S29a†), the WT-EXAFS spectra of Fe in NaFM-F, as shown in Fig. 5c, exhibit two intensity maxima that can assigned to the Fe–O and Fe–TM bonds, respectively.[58] Additionally, the energy position of the XANES spectrum of the Mn K-edge of NaFM-F closely resembles that of MnO_2 (Fig. 5d), indicating that the oxidation state of the isolated Mn atom in NaFM-F is approximately +4.[59] The EXAFS spectra of the Mn atoms of NaFM-F, depicted in Fig. 5e, reveal two distinct peaks at around 1.32 and 2.42 Å, which can be attributed to the Mn–O and Mn–TM bonds, respectively.[60,61] The presence of the Mn–O and Mn–TM bonds in NaFM-F is further supported by the two intensity maxima observed in the WT-EXAFS spectra of Mn in NaFM-F (Fig. 5f), in contrast to the single intensity maximum in the WT-EXAFS spectra of Mn foil, which corresponds to Mn–Mn bonds (Fig. S29b†). In addition, XAFS tests were conducted to investigate the charge compensation mechanism of the ternary NaNFM-F compound. As illustrated in Fig. 5g, the XANES spectrum of the Ni K-edges of NaNFM-F is positioned closer to that of the reference NiO, indicating that the oxidation state of the Ni atom in NaNFM-F is +2.[62] The two peaks observed at approximately 1.50 and 2.49 Å in the EXAFS spectra of the Ni atoms in NaNFM-F correspond to the Ni–O first coordination shell and Ni–

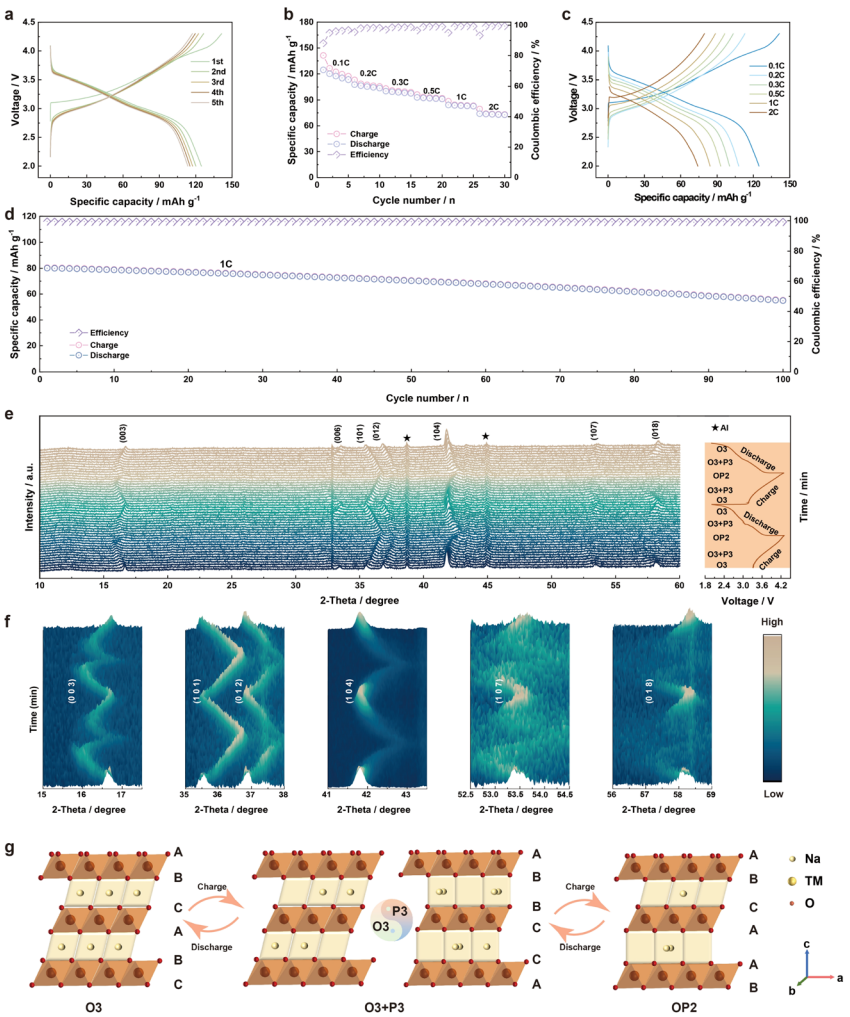

Fig. 6 Electrochemical performance of NaNFM-F within the potential window of 2–4.3 V (a) GCD curves at 0.1 C. (b) Rate performance. (c) GCD curves at different rates. (d) Cycling performance at 1 C. (e) *In situ* XRD patterns of NaNFM-F in the first two cycles at 0.1 C in the potential window of 2.0–4.3 V. (f) The corresponding contour plots. (g) Schematic diagram of the structural evolution process during the Na^+ extraction/insertion.

TM bonds, respectively (Fig. 5j).[63] Compared with the single intensity maximum observed in the WT-EXAFS spectrum of Ni foil (Fig. S29c†), the presence of two intensity maxima in the WT-EXAFS spectrum of Ni in NaNFM-F (Fig. 5m) further corroborates these findings. Similar to the Fe K-edges in NaFM-F, the Fe K-edges of NaNFM-F suggest that the valence state of Fe is +2/+3 (Fig. 5h). Additionally, the EXAFS and WT-EXAFS spectra of Fe in NaNFM-F indicate the presence of the Fe–O and Fe–TM bonds (Fig. 5k and n). Furthermore, analogous results are also observed in the charge mechanisms of Mn in NaNFM-F, as indicated by the XAFS analysis, which demonstrates the near +4 valence state of Mn and the existence of Mn–O bonds and Mn–TM bonds (Fig. 5i, l and o).

Furthermore, a potential window of 2–4.3 V was applied to investigate the electrochemical performance of NaNFM-F over a wider operating voltage range. As illustrated in Fig. 6a–d, within this potential range, NaNFM-F exhibits an initial specific capacity of 124.6 mAh g^{-1} at 0.1 C and demonstrates a rate performance of 74.1 mAh g^{-1} at 2 C, along with a stable cycling performance of 70.0% capacity retention over 100 cycles at 1 C. To gain insight into the evolution of the crystal structure of NaNFM-F during the Na^+ de/intercalation process, *in situ* XRD tests were conducted during the charge and discharge process at 0.1 C within the potential range of 2–4.3 V during the first two cycles. As shown in Fig. 6e, f and S30,† the *in situ* XRD patterns and the corresponding intensity contour maps of the main characteristic diffraction peaks reveal the details of the phase evolution. During Na^+ extraction, the peaks at (003), (006), (107), and (108) shift to a lower angle, indicating an expansion of the *c*-axis of the NaNFM-F crystal structure due to increased electrostatic repulsion from the adjacent TMO_2 layers as the Na^+ is extracted from the lattice.[64] In contrast, the peaks at (101), (012), and (104) shift to higher angles, suggesting a contraction of the *ab* plane caused by charge compensation resulting from Na^+ extraction, which leads to the oxidation of transition metal ions and reduced repulsion among Na^+ ions.[65,66] The phase transition from O3 to O3/P3 occurs during this process. As Na^+ is further extracted from the lattice with the charge potential gradually exceeding 4.1 V, the intensity of the (104) peak decreases significantly, indicating the formation of a new OP2 phase.[67] During the reverse discharge process, the crystal structure undergoes an opposite evolution from OP2 to O3/P3 to O3, and in the second cycle, the crystal structure evolution process resembles that of the initial cycle. As illustrated in Fig. 6g, the structural evolution follows the sequence O3-O3/P3-OP2-O3/P3-O3 during cycling, indicating the excellent structural reversibility of NaNFM-F in the voltage range of 2.0–4.3 V.[68]

Conclusions

In summary, a creative strategy for the preparation of layered oxide cathodes for SIBs with PBAs as precursors is proposed, and the fast sintering strategy has been successfully implemented. The universality of this strategy was demonstrated by verifying the feasibility of converting binary, ternary, and quaternary PBAs into layered oxides. It was found that the conversion from PBAs to layered oxides involves significant structural evolution, transitioning from PBAs to an amorphous state, and ultimately forming layered oxides, as evidenced by a series of advanced characterization experiments. The initially ordered arrangement of the transition metal elements in the PBAs precursor may explain the effectiveness of the fast sintering strategy, as it does not require sustained energy input to maintain an ordered arrangement. Utilizing PBAs as precursors, all the layered oxide cathodes prepared through the fast sintering strategy exhibit electrochemical properties comparable to those produced by the long period sintering process and outperform their PBAs precursors. This "two birds with one stone" strategy not only significantly reduces the energy consumption by shortening the sintering time but also could convert the unqualified PBAs into valuable layered oxides, thereby mitigating environmental pollution. Therefore, this strategy is worthy of further exploration and could be extended to applications beyond SIBs.

Data availability

Essential data are fully provided in the main text and ESI.†

Author contributions

Hong-Wei Li: investigation, data curation, writing of original draft, and formal analysis; Jingqiang Wang: investigation, data curation, and paper revision; Jing Yu: investigation and data curation; Jia-Yang Li: data curation; Yan-Fang Zhu: formal analysis validation and funding acquisition; Huanhuan Dong: project administration and validation; Zhijia Zhang: project administration, Yong Jiang: validation; Shi-Xue Dou: validation; Yao Xiao: paper revision, validation, and funding acquisition.

Conflicts of interest

The authors declare no competing interests.

Acknowledgements

This work was supported by the National Natural Science Foundation of China (52402301, 52472240, and 52202284), the Natural Science Foundation of Zhejiang Province (LQ23E020002), the Wenzhou Key Scientific and Technological Innovation Research Project (ZG2023053), the Natural Science Foundation of Inner Mongolia Autonomous Region (2024QN02014), the China Postdoctoral Science Foundation (2024M751539), and the Post Doctoral Research Fund of Inner Mongolia University (10000-23112101/219).

Notes and references

1 J. Wang, Y. F. Zhu, Y. Su, J. X. Guo, S. Chen, H. K. Liu, S. X. Dou, S. L. Chou and Y. Xiao, Routes to high-performance layered oxide cathodes for sodium-ion batteries, *Chem. Soc. Rev.*, 2024, **53**, 4230–4301.
2 J. Huang, K. Wu, G. Xu, M. Wu, S. Dou and C. Wu, Recent progress and strategic perspectives of inorganic solid

electrolytes: fundamentals, modifications, and applications in sodium metal batteries, *Chem. Soc. Rev.*, 2023, **52**, 4933–4995.

3 B. Peng, Z. Zhou, J. Shi, X. Huang, Y. Li and L. Ma, Earth-Abundant Fe-Mn-Based Compound Cathodes for Sodium-Ion Batteries: Challenges and Progress, *Adv. Funct. Mater.*, 2024, **34**, 2311816.

4 W. Zuo and Y. Yang, Synthesis, Structure, Electrochemical Mechanisms, and Atmospheric Stability of Mn-Based Layered Oxide Cathodes for Sodium Ion Batteries, *Acc. Mater. Res.*, 2022, **3**, 709–720.

5 M. Zhang, L. Qiu, W. Hua, Y. Song, Y. Deng, Z. Wu, Y. Zhu, B. Zhong, S. Chou, S. Dou, Y. Xiao and X. Guo, Formulating Local Environment of Oxygen Mitigates Voltage Hysteresis in Li-Rich Materials, *Adv. Mater.*, 2024, **36**, 2311814.

6 A. Sarkar, Q. Wang, A. Schiele, M. R. Chellali, S. S. Bhattacharya, D. Wang, T. Brezesinski, H. Hahn, L. Velasco and B. Breitung, High-Entropy Oxides: Fundamental Aspects and Electrochemical Properties, *Adv. Mater.*, 2019, **31**, 1806236.

7 L.-Y. Kong, H.-X. Liu, Y.-F. Zhu, J.-Y. Li, Y. Su, H.-W. Li, H.-Y. Hu, Y.-F. Liu, M.-J. Yang, Z.-C. Jian, X.-B. Jia, S.-L. Chou and Y. Xiao, Layered oxide cathodes for sodium-ion batteries: microstructure design, local chemistry and structural unit, *Sci. China Chem.*, 2023, **67**, 191–213.

8 H. Li, H. Wang, D. Chan, Z. Xu, K. Wang, M. Ge, Y. Zhang, S. Chen and Y. Tang, Nature-inspired materials and designs for flexible lithium-ion batteries, *Carbon Energy*, 2022, **4**, 878–900.

9 J. Wang, T. H. Nguyen, K. Dong, D. T. Tran, N. H. Kim and J. H. Lee, Engineering dual MoC–Mo_2C heterostructure–knotted CNTs for efficient direct seawater electrolysis, *Int. J. Hydrogen Energy*, 2024, **49**, 1005–1013.

10 S. Xin, X. Zhang, L. Wang, H. Yu, X. Chang, Y.-M. Zhao, Q. Meng, P. Xu, C.-Z. Zhao, J. Chen, H. Lu, X. Kong, J. Wang, K. Chen, G. Huang, X. Zhang, Y. Su, Y. Xiao, S.-L. Chou, S. Zhang, Z. Guo, A. Du, G. Cui, G. Yang, Q. Zhao, L. Dong, D. Zhou, F. Kang, H. Hong, C. Zhi, Z. Yuan, X. Li, Y. Mo, Y. Zhu, D. Yu, X. Lei, J. Zhao, J. Wang, D. Su, Y.-G. Guo, Q. Zhang, J. Chen and L.-J. Wan, Roadmap for rechargeable batteries: present and beyond, *Sci. China Chem.*, 2023, **67**, 13–42.

11 J. Wang, D. T. Tran, K. Chang, S. Prabhakaran, J. Zhao, D. H. Kim, N. H. Kim and J. H. Lee, Hierarchical Ni@CNTs-bridged Mo_xC/Ni_2P heterostructure micro-pillars for enhanced seawater splitting and Mg/seawater battery, *Nano Energy*, 2023, **111**, 108440.

12 C. Liu, K. Chen, H. Xiong, A. Zhao, H. Zhang, Q. Li, X. Ai, H. Yang, Y. Fang and Y. Cao, A novel $Na_8Fe_5(SO_4)_9$@rGO cathode material with high rate capability and ultra-long lifespan for low-cost sodium-ion batteries, *eScience*, 2024, **4**, 100186.

13 K. Chayambuka, G. Mulder, D. L. Danilov and P. H. L. Notten, From Li-Ion Batteries toward Na-Ion Chemistries: Challenges and Opportunities, *Adv. Energy Mater.*, 2020, **10**, 2001310.

14 K. M. Abraham, How Comparable Are Sodium-Ion Batteries to Lithium-Ion Counterparts?, *ACS Energy Lett.*, 2020, **5**, 3544–3547.

15 M. Li, J. Lu, Z. Chen and K. Amine, 30 Years of Lithium-Ion Batteries, *Adv. Mater.*, 2018, **30**, 1800561.

16 Y. J. Guo, R. X. Jin, M. Fan, W. P. Wang, S. Xin, L. J. Wan and Y. G. Guo, Sodium layered oxide cathodes: properties, practicality and prospects, *Chem. Soc. Rev.*, 2024, **53**, 7828–7874.

17 X. Liang, J. Y. Hwang and Y. K. Sun, Practical Cathodes for Sodium-Ion Batteries: Who Will Take The Crown?, *Adv. Energy Mater.*, 2023, **13**, 2301975.

18 X. Xiang, K. Zhang and J. Chen, Recent Advances and Prospects of Cathode Materials for Sodium-Ion Batteries, *Adv. Mater.*, 2015, **27**, 5343–5364.

19 Y.-S. Hu and Y. Li, Unlocking Sustainable Na-Ion Batteries into Industry, *ACS Energy Lett.*, 2021, **6**, 4115–4117.

20 A. Sarkar, Q. Wang, A. Schiele, M. R. Chellali, S. S. Bhattacharya, D. Wang, T. Brezesinski, H. Hahn, L. Velasco and B. Breitung, High-Entropy Oxides: Fundamental Aspects and Electrochemical Properties, *Adv. Mater.*, 2019, **31**, 1806236.

21 S. Xu, H. Dong, D. Yang, C. Wu, Y. Yao, X. Rui, S. Chou and Y. Yu, Promising Cathode Materials for Sodium-Ion Batteries from Lab to Application, *ACS Cent. Sci.*, 2023, **9**, 2012–2035.

22 X. H. Liu, J. Peng, W. H. Lai, Y. Gao, H. Zhang, L. Li, Y. Qiao and S. L. Chou, Advanced Characterization Techniques Paving the Way for Commercialization of Low-Cost Prussian Blue Analog Cathodes, *Adv. Funct. Mater.*, 2021, **32**, 2108616.

23 W. Shu, J. Li, G. Zhang, J. Meng, X. Wang and L. Mai, Progress on Transition Metal Ions Dissolution Suppression Strategies in Prussian Blue Analogs for Aqueous Sodium-/Potassium-Ion Batteries, *Nanomicro Lett*, 2024, **16**, 128.

24 S. Chu, S. Guo and H. Zhou, Advanced cobalt-free cathode materials for sodium-ion batteries, *Chem. Soc. Rev.*, 2021, **50**, 13189–13235.

25 X. B. Jia, J. Wang, Y. F. Liu, Y. F. Zhu, J. Y. Li, Y. J. Li, S. L. Chou and Y. Xiao, Facilitating Layered Oxide Cathodes Based on Orbital Hybridization for Sodium-Ion Batteries: Marvelous Air Stability, Controllable High Voltage, and Anion Redox Chemistry, *Adv. Mater.*, 2024, **36**, 2307938.

26 W. Zuo, A. Innocenti, M. Zarrabeitia, D. Bresser, Y. Yang and S. Passerini, Layered Oxide Cathodes for Sodium-Ion Batteries: Storage Mechanism, Electrochemistry, and Techno-economics, *Acc. Chem. Res.*, 2023, **56**, 284–296.

27 X. Rong, D. Xiao, Q. Li, Y. Niu, F. Ding, X. Hou, Q. Wang, J. Xu, C. Zhao, D. Zhou, R. Xiao, X. Yu, Y. Wen, L. Gu, H. Li, X. Huang, L. Chen and Y. S. Hu, "Boosting Reversible Anionic Redox Reaction with Li/Cu Dual Honeycomb Centers", *eScience.*, 2023, **3**, 100159.

28 L. Y. Kong, J. Y. Li, H. X. Liu, Y. F. Zhu, J. Wang, Y. Liu, X. Y. Zhang, H. Y. Hu, H. Dong, Z. C. Jian, C. Cheng, S. Chen, L. Zhang, J. Z. Wang, S. Chou and Y. Xiao, A Universal Interfacial Reconstruction Strategy Based on

Converting Residual Alkali for Sodium Layered Oxide Cathodes: Marvelous Air Stability, Reversible Anion Redox, and Practical Full Cell, *J. Am. Chem. Soc.*, 2024, **146**, 32317–32332.

29 C. Delmas, D. Carlier and M. Guignard, The Layered Oxides in Lithium and Sodium-Ion Batteries: A Solid-State Chemistry Approach, *Adv. Energy Mater.*, 2020, **11**, 2001201.

30 L. Zhang, C. Guan, Y. Xie, H. Li, A. Wang, S. Chang, J. Zheng, Y. Lai and Z. Zhang, Heteroatom-Substituted P2-$Na_{2/3}Ni_{1/4}Mg_{1/12}Mn_{2/3}O_2$ Cathode with {010} Exposing Facets Boost Anionic Activity and High-Rate Performance for Na-Ion Batteries, *ACS Appl. Mater. Interfaces*, 2022, **14**, 18313–18323.

31 Z. C. Jian, J. X. Guo, Y. F. Liu, Y. F. Zhu, J. Wang and Y. Xiao, Cation migration in layered oxide cathodes for sodium-ion batteries: fundamental failure mechanisms and practical modulation strategies, *Chem. Sci.*, 2024, **15**, 19698–19728.

32 Z. Qin, Y. Zhang, W. Luo, T. Zhang, T. Wang, L. Ni, H. Wang, N. Zhang, X. Liu, J. Zhou and G. Chen, A Universal Molten Salt Method for Direct Upcycling of Spent Ni-rich Cathode towards Single-crystalline Li-rich Cathode, *Angew. Chem., Int. Ed.*, 2023, **62**, e202218672.

33 M. Zhou, J. Shen, Y. Zuo, R. Liu, J. Zhao and G. Zhou, The Fischer-Lactonization-Driven Mechanism for Ultra-Efficient Recycling of Spent Lithium-Ion Batteries, *Angew. Chem., Int. Ed.*, 2024, e202414484.

34 L. L. Driscoll, A. Jarvis, R. Madge, E. H. Driscoll, J.-M. Price, R. Sommerville, F. S. Tontini, M. Bahri, M. Miah, B. L. Mehdi, E. Kendrick, N. D. Browning, P. K. Allan, P. A. Anderson and P. R. Slater, Phase-selective recovery and regeneration of end-of-life electric vehicle blended cathodes *via* selective leaching and direct recycling, *Joule*, 2024, **8**, 2735–2754.

35 L. Duan, H. Tang, X. Xu, J. Liao, X. Li, G. Zhou and X. Zhou, MnFe Prussian blue analogue-derived P3-$K_{0.5}Mn_{0.67}Fe_{0.33}O_{1.95}N_{0.05}$ cathode material for high-performance potassium-ion batteries, *Energy Storage Mater.*, 2023, **62**, 102950.

36 Z.-C. Jian, Y.-F. Liu, Y.-F. Zhu, J.-Y. Li, H.-Y. Hu, J. Wang, L.-Y. Kong, X.-B. Jia, H.-X. Liu, J.-X. Guo, M.-Y. Li, Y.-S. Xu, J.-F. Mao, S.-L. Zhang, Y. Su, S.-X. Dou, S.-L. Chou and Y. Xiao, Solid-state synthesis of low-cost and high-energy-density sodium layered-tunnel oxide cathodes: Dynamic structural evolution, Na^+/vacancy disordering, and prominent moisture stability, *Nano Energy*, 2024, **125**, 109528.

37 S. Xu, H. Chen, X. Zhang, M. Zhou and H. Zhou, NASICON-Type $NaTi_2(PO_4)_3$ Surface Modified O3-Type $NaNi_{0.3}Fe_{0.2}Mn_{0.5}O_2$ for High-Performance Cathode Material for Sodium-Ion Batteries, *ACS Appl. Mater. Interfaces*, 2023, **15**, 47764–47778.

38 Y. Li, Z. Xu, X. Zhang, Z. Wu, J.-E. Zhou, J. Zhang and X. Lin, Tuning the electrochemical behaviors of N-doped $LiMn_xFe_{1-x}PO_4$/C *via* cation engineering with metal-organic framework-templated strategy, *J. Energy Chem.*, 2023, **85**, 239–253.

39 Z. Zhang, Y. Liu, Z. Liu, H. Li, Y. Huang, W. Liu, D. Ruan, X. Cai and X. Yu, Dual-strategy of Cu-doping and O3 biphasic structure enables Fe/Mn-based layered oxide for high-performance sodium-ion batteries cathode, *J. Power Sources*, 2023, **567**, 232930.

40 H. Y. Hu, H. Wang, Y. F. Zhu, J. Y. Li, Y. Liu, J. Wang, H. X. Liu, X. B. Jia, H. Li, Y. Su, Y. Gao, S. Chen, X. Wu, S. X. Dou, S. Chou and Y. Xiao, A Universal Strategy Based on Bridging Microstructure Engineering and Local Electronic Structure Manipulation for High-Performance Sodium Layered Oxide Cathodes, *ACS Nano*, 2023, **17**, 15871–15882.

41 J. Jiao, K. Wu, N. Li, E. Zhao, W. Yin, Z. Hu, F. Wang, J. Zhao and X. Xiao, Tuning anionic redox activity to boost high-performance sodium-storage in low-cost $Na_{0.67}Fe_{0.5}Mn_{0.5}O_2$ cathode, *J. Energy Chem.*, 2022, **73**, 214–222.

42 C. Wang, L. Liu, S. Zhao, Y. Liu, Y. Yang, H. Yu, S. Lee, G. H. Lee, Y. M. Kang, R. Liu, F. Li and J. Chen, Tuning local chemistry of P2 layered-oxide cathode for high energy and long cycles of sodium-ion battery, *Nat. Commun.*, 2021, **12**, 2256.

43 N. Jiang, Q. Liu, J. Wang, W. Yang, W. Ma, L. Zhang, Z. Peng and Z. Zhang, Tailoring P2/P3 Biphases of Layered Na_xMnO_2 by Co Substitution for High-Performance Sodium-Ion Battery, *Small*, 2021, **17**, 2007103.

44 X. G. Yuan, Y. J. Guo, L. Gan, X. A. Yang, W. H. He, X. S. Zhang, Y. X. Yin, S. Xin, H. R. Yao, Z. Huang and Y. G. Guo, A Universal Strategy toward Air-Stable and High-Rate O3 Layered Oxide Cathodes for Na-Ion Batteries, *Adv. Funct. Mater.*, 2022, **32**, 2111466.

45 H. W. Li, J. Y. Li, H. H. Dong, Y. F. Zhu, Y. Su, J. Q. Wang, Y. N. Liu, C. Y. Wen, Z. J. Wang, S. Q. Chen, Z. J. Zhang, J. Z. Wang, Y. Jiang, S. L. Chou and Y. Xiao, An Intrinsic Stable Layered Oxide Cathode for Practical Sodium-Ion Battery: Solid Solution Reaction, Near-Zero-Strain and Marvelous Water Stability, *Small*, 2024, **20**, 2306690.

46 J. Peng, Y. Gao, H. Zhang, Z. Liu, W. Zhang, L. Li, Y. Qiao, W. Yang, J. Wang, S. Dou and S. Chou, Ball Milling Solid-State Synthesis of Highly Crystalline Prussian Blue Analogue $Na_{2-x}MnFe(CN)_6$ Cathodes for All-Climate Sodium-Ion Batteries, *Angew. Chem., Int. Ed.*, 2022, **61**, e202205867.

47 Y.-h. Luo, Q.-l. Pan, H.-x. Wei, Y.-d. Huang, L.-b. Tang, Z.-y. Wang, C. Yan, J. Mao, K.-h. Dai, Q. Wu, X.-h. Zhang and J.-c. Zheng, Regulating cation mixing for enhanced structural stability of layered oxide cathodes by ion-exchange strategy, *Mater. Today*, 2023, **69**, 54–65.

48 S. S. Aamlid, M. Oudah, J. Rottler and A. M. Hallas, Understanding the Role of Entropy in High Entropy Oxides, *J. Am. Chem. Soc.*, 2023, **145**, 5991–6006.

49 Z. Li, W. Kong, Y. Yu, J. Zhang, D. Wong, Z. Xu, Z. Chen, C. Schulz, M. Bartkowiak and X. Liu, Tuning Bulk O_2 and Nonbonding Oxygen State for Reversible Anionic Redox Chemistry in P2-Layered Cathodes, *Angew. Chem., Int. Ed.*, 2022, **61**, e202115552.

50 H. Yang, D. Wang, Y. Liu, Y. Liu, B. Zhong, Y. Song, Q. Kong, Z. Wu and X. Guo, Improvement of cycle life for layered oxide cathodes in sodium-ion batteries, *Energy Environ. Sci.*, 2024, **17**, 1756–1780.

51 S. Jia, S. Kumakura and E. McCalla, Unravelling air/moisture stability of cathode materials in sodium ion batteries: characterization, rational design, and perspectives, *Energy Environ. Sci.*, 2024, **17**, 4343–4389.

52 C. Li, A. Li, M. Li, P. Xiong, Y. Liu, M. Cheng, D. Geng and Y. Xu, Ultrafast Synthesis of Layered Transition-Metal Oxide Cathodes from Metal-Organic Frameworks for High-Capacity Sodium-Ion Batteries, *ACS Appl. Mater. Interfaces*, 2022, **14**, 24462–24468.

53 W. Zhu, J. Zhang, J. Luo, C. Zeng, H. Su, J. Zhang, R. Liu, E. Hu, Y. Liu, W. D. Liu, Y. Chen, W. Hu and Y. Xu, Ultrafast Non-Equilibrium Synthesis of Cathode Materials for Li-Ion Batteries, *Adv. Mater.*, 2023, **35**, 2208974.

54 J. Wang, Q.-Q. Sun, J. Yu, J.-X. Guo, N.-K. Mo, H.-W. Li, Y. Su, S. Zhao, Y.-F. Zhu, H. Chu, S. Dou and Y. Xiao, Constructing layered/tunnel interlocking oxide cathodes for sodium-ion batteries based on breaking Mn^{3+}/Mn^{4+} equilibrium in $Na_{0.44}MnO_2$ *via* trace Mo doping, *Compos. Part B Eng.*, 2024, **284**, 111664.

55 T. Yang, D. Luo, X. Zhang, S. Gao, R. Gao, Q. Ma, H. W. Park, T. Or, Y. Zhang and Z. Chen, Sustainable regeneration of spent cathodes for lithium-ion and post-lithium-ion batteries, *Nat. Sustain.*, 2024, **7**, 776–785.

56 X. L. Li, T. Wang, Y. Yuan, X. Y. Yue, Q. C. Wang, J. Y. Wang, J. Zhong, R. Q. Lin, Y. Yao, X. J. Wu, X. Q. Yu, Z. W. Fu, Y. Y. Xia, X. Q. Yang, T. Liu, K. Amine, Z. Shadike, Y. N. Zhou and J. Lu, Whole-Voltage-Range Oxygen Redox in P2-Layered Cathode Materials for Sodium-Ion Batteries, *Adv. Mater.*, 2021, **33**, 2008194.

57 N. Hong, J. Li, H. Wang, X. Hu, B. Zhao, F. Hua, Y. Mei, J. Huang, B. Zhang, W. Jian, J. Gao, Y. Tian, X. Shi, W. Deng, G. Zou, H. Hou, Z. Hu, Z. Long and X. Ji, Regulating Phase Transition and Restraining Fe Distortion at High Potential Window *via* Rare Earth Metal Incorporation on O3-Type Layered Cathodes, *Adv. Funct. Mater.*, 2024, **34**, 2402398.

58 X. Wang, Q. Zhang, C. Zhao, H. Li, B. Zhang, G. Zeng, Y. Tang, Z. Huang, I. Hwang, H. Zhang, S. Zhou, Y. Qiu, Y. Xiao, J. Cabana, C.-J. Sun, K. Amine, Y. Sun, Q. Wang, G.-L. Xu, L. Gu, Y. Qiao and S.-G. Sun, Achieving a high-performance sodium-ion pouch cell by regulating intergrowth structures in a layered oxide cathode with anionic redox, *Nat. Energy*, 2024, **9**, 184–196.

59 J. H. Jo, H. J. Kim, J. U. Choi, N. Voronina, K.-S. Lee, K. Ihm, H.-K. Lee, H.-D. Lim, H. Kim, H.-G. Jung, K. Y. Chung, H. Yashiro and S.-T. Myung, Facilitating sustainable oxygen-redox chemistry for P3-type cathode materials for sodium-ion batteries, *Energy Storage Mater.*, 2022, **46**, 329–343.

60 G. Chen, H. Ji, H. Fang, J. Zhai, Z. Ma, W. Ji, Y. Wang, Y. Huang, L. Liu, W. Tong, W. Zeng and Y. Xiao, Dual Modification of P3-Type Layered Cathodes to Achieve High Capacity and Long Cyclability for Sodium-Ion Batteries, *ACS Appl. Mater. Interfaces*, 2023, **15**, 33682–33692.

61 Q. Huang, J. Liu, L. Zhang, S. Xu, L. Chen, P. Wang, D. G. Ivey and W. Wei, Tailoring alternating heteroepitaxial nanostructures in Na-ion layered oxide cathodes *via* an *in situ* composition modulation route, *Nano Energy*, 2018, **44**, 336–344.

62 D. S. Bhange, G. Ali, D.-H. Kim, D. A. Anang, T. J. Shin, M.-G. Kim, Y.-M. Kang, K. Y. Chung and K.-W. Nam, Honeycomb-layer structured $Na_3Ni_2BiO_6$ as a high voltage and long life cathode material for sodium-ion batteries, *J. Mater. Chem. A*, 2017, **5**, 1300–1310.

63 Q. Wang, D. Zhou, C. Zhao, J. Wang, H. Guo, L. Wang, Z. Yao, D. Wong, G. Schuck, X. Bai, J. Lu and M. Wagemaker, Fast-charge high-voltage layered cathodes for sodium-ion batteries, *Nat. Sustain*, 2024, **7**, 338–347.

64 H. Wang, X. Gao, S. Zhang, Y. Mei, L. Ni, J. Gao, H. Liu, N. Hong, B. Zhang, F. Zhu, W. Deng, G. Zou, H. Hou, X.-Y. Cao, H. Chen and X. Ji, High-Entropy Na-Deficient Layered Oxides for Sodium-Ion Batteries, *ACS Nano*, 2023, **17**, 12530–12543.

65 L. Yu, Z. Cheng, K. Xu, Y.-X. Chang, Y.-H. Feng, D. Si, M. Liu, P.-F. Wang and S. Xu, Interlocking biphasic chemistry for high-voltage P2/O3 sodium layered oxide cathode, *Energy Storage Mater.*, 2022, **50**, 730–739.

66 J. Mu, T. Cai, W. Dong, C. Zhou, Z. Han and F. Huang, Biphasic high-entropy layered oxide as a stable and high-rate cathode for sodium-ion batteries, *Chem. Eng. J.*, 2023, **471**, 144403.

67 P. Zhou, Z. Che, J. Liu, J. Zhou, X. Wu, J. Weng, J. Zhao, H. Cao, J. Zhou and F. Cheng, High-entropy P2/O3 biphasic cathode materials for wide-temperature rechargeable sodium-ion batteries, *Energy Storage Mater.*, 2023, **57**, 618–627.

68 J. Li, H. Hu, J. Wang and Y. Xiao, Surface chemistry engineering of layered oxide cathodes for sodium-ion batteries, *Carbon Neutralization*, 2022, **1**, 96–116.